Additive Manufacturing xxx (xxxx) xxx

Contents lists available at ScienceDirect

Additive Manufacturing

journal homepage: www.elsevier.com/locate/addma

Research Paper

The influence of columnar to equiaxed transition on deformation behavior of FeCoCrNiMn high entropy alloy fabricated by laser-based directed energy deposition

Mengyao Zheng [a], Chuanwei Li [a,*], Xinyu Zhang [a], Zhenhua Ye [a], Xudong Yang [a], Jianfeng Gu [a,b,**]

[a] Institute of Materials Modification and Modelling, School of Materials Science and Engineering, Shanghai Jiao Tong University, Shanghai 200240, China
[b] Shanghai Key Laboratory of Materials Laser Processing and Modification, Shanghai Jiao Tong University, Shanghai 200240, China

ARTICLE INFO

Keywords:
High entropy alloys
Directed energy deposition
Columnar to equiaxed transition
Strengthening mechanisms
Deformation behavior

ABSTRACT

This study investigates the columnar to equiaxed transition (CET) and deformation behavior of a FeCoCrNiMn high entropy alloy (HEA) fabricated by laser-based directed energy deposition (DED). The results show that two kinds of microstructure can be obtained in the as-built HEAs by changing laser scanning speed: one kind of microstructure is formed at a low scanning speed and composed of near fully equiaxed grains; the other is formed at a high scanning speed and composed of columnar grains. These two different microstructures are closely related to the CET, which is decided by the ratio of thermal gradient and solidification rate in the molten pool. Additionally, compared with traditional HEAs, as-built HEAs show a heterogeneous grain-size distribution and high dislocation density, as well as improved tensile properties, one of which (Yield strength = 330 MPa; Ultimate tensile strength = 630 MPa; Fracture elongation = 55%) is similar to the properties of wrought HEAs. Moreover, the as-built HEA with equiaxed grains shows a higher work hardening rate than the as-built HEA with columnar grains and the equiaxed microstructure has the characteristics of intergranular microcracks, the columnar microstructure shows the characteristics of intragranular microcracks. The deformation behavior was investigated using *in-situ* high-resolution digital image correlation methods, and the result shows that the difference in work hardening rate is closely related to the texture formed during deposition.

1. Introduction

Since the high entropy alloy (HEA) was investigated at the beginning of this century, it has received more and more attention from scholars because of its excellent properties [1–5]. The equiatomic FeCoCrNiMn HEA was proposed by Cantor [2] in 2004. It has a single-phase face-centered cubic (FCC) structure and is the most widely studied HEA system. The yield strength, ultimate tensile strength and ductility of FeCoCrNiMn HEA simultaneously increase with the decrease of temperature, the results show the increasing of ductility is because of the occurrence of dislocation glide and mechanical twinning in the early stage of tensile test at cryogenic temperature [3,6,7]. However, the mechanical twinning is activated in the late stage of deformation at room temperature [6,7]. By refining grains at room temperature, it can obtain excellent comprehensive mechanical properties with tensile strength of 650 MPa and fracture elongation of 60% [8]. Moreover, Pickering et al. [9] show σ phase will be precipitated after holding at 700 °C for more than 500 h in the homogenization state FeCoCrNiMn HEA , but the research of Klimova et al. [10] show the Cr-rich body-centered-cubic phase and sigma phase can be precipitated after annealing at 500–800 °C for only 1 h in the cold-worked FeCoCrNiMn alloy, and these second phase particles effectively enhance the strength. These excellent properties make the FeCoCrNiMn HEA a good candidate for the application in extreme environments. Bulk HEAs are mainly prepared by the traditional melting and casting process. However, this method requires re-melting of materials to ensure a uniform composition and does not easily obtain complex-shape components, which increases the complexity of preparation process and impedes the practical

* Corresponding author.
** Corresponding author at: Institute of Materials Modification and Modelling, School of Materials Science and Engineering, Shanghai Jiao Tong University, Shanghai 200240, China.
E-mail addresses: li-chuanwei@sjtu.edu.cn (C. Li), gujf@sjtu.edu.cn (J. Gu).

https://doi.org/10.1016/j.addma.2020.101660
Received 14 June 2020; Received in revised form 21 September 2020; Accepted 8 October 2020
Available online 14 October 2020

application of the alloys [11]. Fortunately, there is a newly developed manufacturing process—Additive Manufacturing (AM).

AM as a high-flexibility and near-net-shape process, has attracted much attention in various fields [12]. Laser-based directed energy deposition (DED) is one of the AM processes, and its deposition process is similar with that of laser welding. Compared with the traditional arc-melting process, laser-based process has the following characteristics: (1) an extremely fast cooling rate; (2) local melting; (3) directional solidification; (4) remelting and reheating. Recently, more and more researches of laser processed HEAs have been carried out [13–19], and some papers have reported the microstructure, mechanical properties and strengthening mechanisms of additively manufactured FeCoCrNiMn HEA [15,16,19,20], but there is still a lack of systematic research on the relationship between the manufacturing process, and the microstructures and properties. The columnar to equiaxed transition (CET), which is widely observed in additively manufactured metal materials [21,22], has also been reported in FeCoCrNiMn HEA. However, the controlling of CET, the different CET behavior between FeCoCrNiMn HEA and traditional alloys, and the impact of CET on the microstructure and properties of HEA have not been addressed in detail. Therefore, more systematic research about the CET of HEA need to be carried out.

In this work, FeCoCrNiMn HEAs were prepared by a laser-based DED process. By using different process parameters, the CET process was controlled. The formation mechanisms of microstructures, the influence of microstructure on the mechanical properties and deformation behavior of AM-FeCoCrNiMn HEA were investigated.

2. Experimental

2.1. Material and processing

FeCoCrNiMn pre-alloyed powder with a particle size of 50–110 μm was prepared by electrode induction melting gas atomization (EIGA). Its morphology, chemical composition and crystal structure are shown in Fig. 1(a) and (b). The thin-wall shaped bulk HEAs (40 mm × 2 mm × 70 mm) were fabricated on a FeCoCrNiMn HEA substrate by a coaxial powder feeding DED system equipped with ytterbium fiber laser, and the deposition process was carried out in a cavity filled with high-purity Ar gas. The scanning strategy is shown in Fig. 1(c). The process parameters are shown in Table 1, the linear energy density is used in this study:

$$E = P/v \quad (1)$$

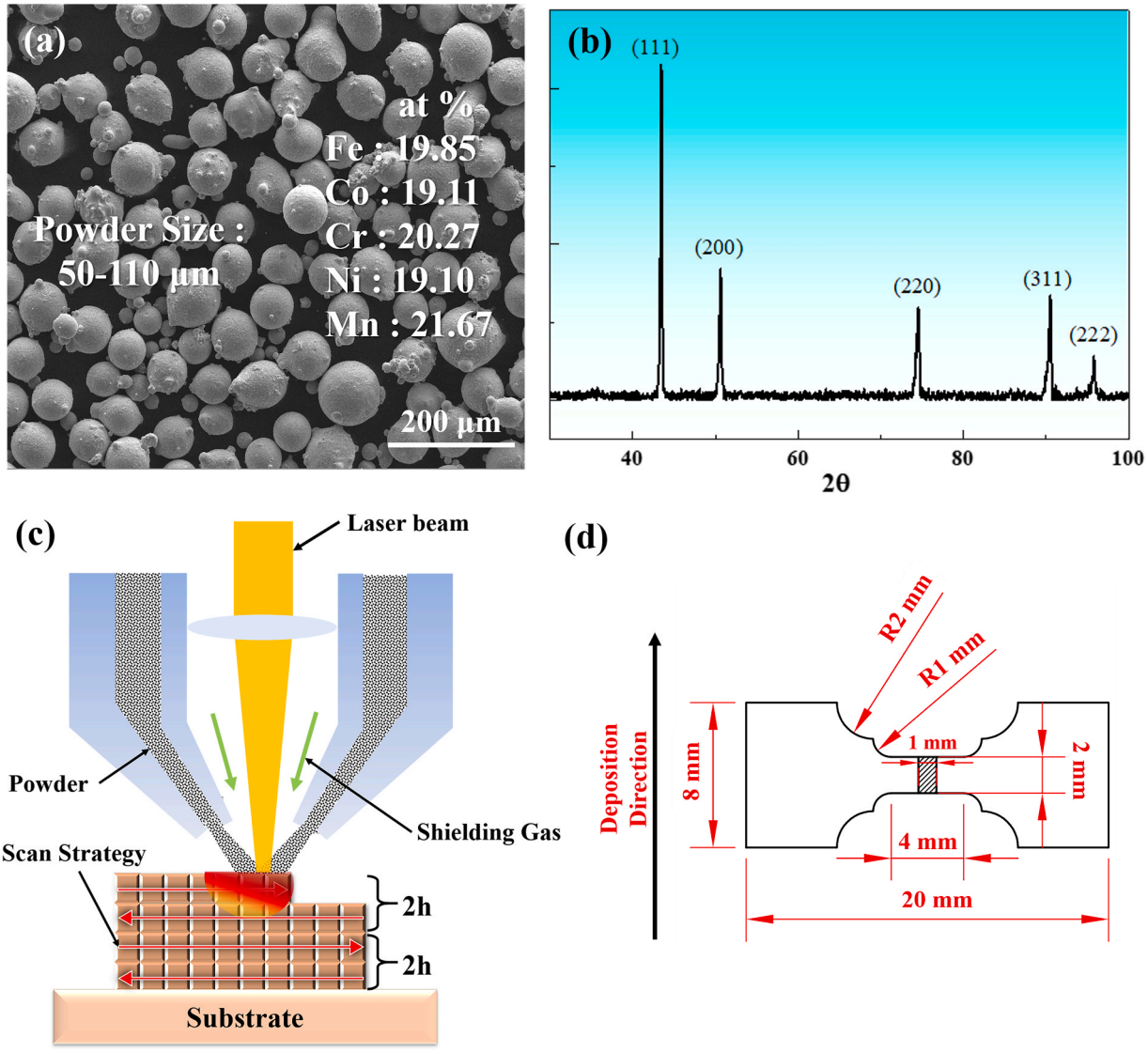

Fig. 1. (a) Morphology of FeCoCrNiMn HEA powder; (b) XRD of FeCoCrNiMn HEA powder; (c) schematic diagram of DED process and laser scan strategy; (d) dimensions of tensile sample.

Table 1
DED process parameters of FeCoCrNiMn HEAs.

Sample	Laser power (W)	Scan speed (mm/s)	Z-axis increment (mm)	Powder feeding rate (g/min)	Linear energy density (J/mm)
AM-200–3	200	3	0.4	5.7	66.7
AM-200–4	200	4		6.8	50.0
AM-300–3	300	3		5.7	100
AM-300–5	300	5		6.8	60
AM-400–3	400	3		5.7	133.3
AM-400–5	400	5		6.8	80

where P is the laser power (W), v is the scanning speed (mm/s).

The as-built samples are named "AM (additive manufacturing)-laser power-scanning speed", for example, AM-200–3 means the sample was fabricated by using the parameters: P = 300 W, and V = 3 mm/s. For comparison, a bulk FeCoCrNiMn HEA was also fabricated by vacuum arc melting and water-cooling copper mold suction casting, which can also obtain extremely fast cooling rates. The suction-cast samples are named "SC".

2.2. Mechanical and in-Situ deformation testing

Flat dog-bone shaped tensile samples with gauge dimensions of 1 mm × 2 mm × 4 mm (thickness × width × length) were machined by electrical discharge machining. The tensile axis of the as-built samples is perpendicular to the deposition direction, as shown in Fig. 1(d). The suction casting tensile samples were taken near the surface where the cooling rate was fast. Three samples were tensile-tested for each condition.

Room-temperature and *in-situ* high-resolution digital image correlation (HR-DIC) tensile tests were carried out under a field-emission scanning electron microscope (SEM, LYRA3 GMU, TESCAN, Czech Republic) equipped with a tensile machine (MICROTEST 5 kN water-cooled, Gatan, United Kingdom), at a tensile rate of 0.1 mm/min. The engineering strain during tensile test was calculated by the DIC method. For HR-DIC test, speckle particles on the surface of the tensile samples were obtained by using the method proposed by Gioacchino et al. [23]. And the SEM image size was 8192 × 6144 pixels, the dwell time of the image was 3.2 μs, and the field size was 138 × 104 μm^2, resulting in an image resolution of 17 nm/pixel. The strain maps of HR-DIC were calculated with VIC2D software (Correlated Solutions, USA). The subset and step sizes for image correlation were 29 pixels (~493 nm) and 7 pixels (~119 nm), respectively. After the test, the speckle was removed for the subsequent EBSD scanning by using 0.02 μm colloidal silica (OPS) solution.

2.3. Material characterization

The microstructure characterization was performed using optical microscope (OM, Axio Observer A1, Zeiss, Germany) and SEM. The samples for OM observation were etched using an aqua regia solution (HNO_3:HCL = 1:3). Electron backscatter diffraction (EBSD, Nordlys-Max3, Oxford Instruments, United Kingdom) was carried out under the field-emission SEM, undeformed samples were tested with two scanning strategies, 800 μm × 800 μm and 200 μm × 200 μm, with a step size of 0.8 μm and 0.4 μm, respectively, and the step size of deformed samples was 0.1 μm. The content of five principal elements (Fe/Co/Cr/Ni/Mn) were analyzed using the energy disperse spectroscopy (EDS) detector included in the SEM, and the content of impurities (C/O/N/S) were checked by combustion furnace analysis and carbon sulfur analyzer. X-ray diffraction (XRD, D8 ADVANCE Da Vinci, Bruker, Germany) was used to analyze the crystal structure and dislocation density of the samples. The samples for EBSD and XRD detection were electropolished at −30 °C and 25 V with 7% perchloric acid and 93% ethanol solution for 40 s. A JEM-2100F transmission electron microscope (TEM, JEOL, Japan) was used to investigate the microstructure in more detail. The thin film samples used for TEM were prepared by twin-jet electronic polishing method at −25 °C with 7% perchloric acid and 93% ethanol solution.

3. Results

3.1. Microstructure characterization

The composition of the FeCoCrNiMn HEAs is listed in Table 2 and Table. S1, it can be seen that the composition of SC and as-built HEAs are near equiatomic, but the oxygen content of as-built samples is higher than that of SC.

Fig. 2(a)–(g) shows BSE images of the SC and as-built FeCoCrNiMn HEAs. The observation surface of as-built samples is X (scanning direction)–Z (deposition direction) plane, which is shown at the bottom right of Fig. 2. It can be seen that the microstructure of as-built samples is different from SC. The grain morphology of as-built samples is very irregular, and distribution of grain size is heterogeneous, whereas the SC obtained equiaxed grains with homogeneous grain size distribution near the cooling surface. In addition, owing to the different processing parameters, there are two-type microstructures in the as-built samples. As shown in Fig. 2(a), (b) and (c), at a low scanning speed, the type I microstructure was obtained, the grain morphology is similar to equiaxed grains and there is no epitaxial growth between adjacent layers. In contrast, when the scanning speed increases, obvious columnar grains appear in the type II microstructure, the grain morphology shows the characteristics of "Zigzag" epitaxial growth through multiple layers, as shown in Fig. 2(d), (e) and (f). The epitaxial-growth microstructure also exists in the laser deposited nickel-base superalloy and the 316 L stainless steel [24–26]. Fig. 2(h) shows the XRD patterns of FeCoCrNiMn HEAs, it can be seen the SC and as-built HEAs are single-phase FCC structure.

Fig. 3 shows the dendrite structure of SC and two typical as-built HEAs (AM-200–3 and AM-200–4) after etched. From Fig. 3(a)–(c), it can be seen that the dendrite morphology of the three samples is different. Fig. 3(d)–(f) shows the magnified view of the dendrite structure. The SC is composed of columnar dendrites circled by the green ellipse in Fig. 3(d), and the dendrite structures of AM-200–3 and AM-200–4 are equiaxed and cellular dendrites, respectively. The red lines in Fig. 3(f)–(h) are the grain boundaries. For the columnar dendrites existed in the SC, the primary dendrite spacing is equivalent to the grain

Table 2
Chemical composition of suction-casting and as-built FeCoCrNiMn HEAs.

Composition (at%)	Fe	Co	Cr	Ni	Mn	C	O	N	S
AM-200–3	19.92	19.77	20.43	19.14	20.74	0.014	0.044	0.011	0.010
AM-200–4	20.15	19.75	20.30	19.35	20.45	0.005	0.041	0.012	0.010
SC	19.81	19.70	20.52	19.13	20.66	0.029	0.0007	<0.0010	0.0061

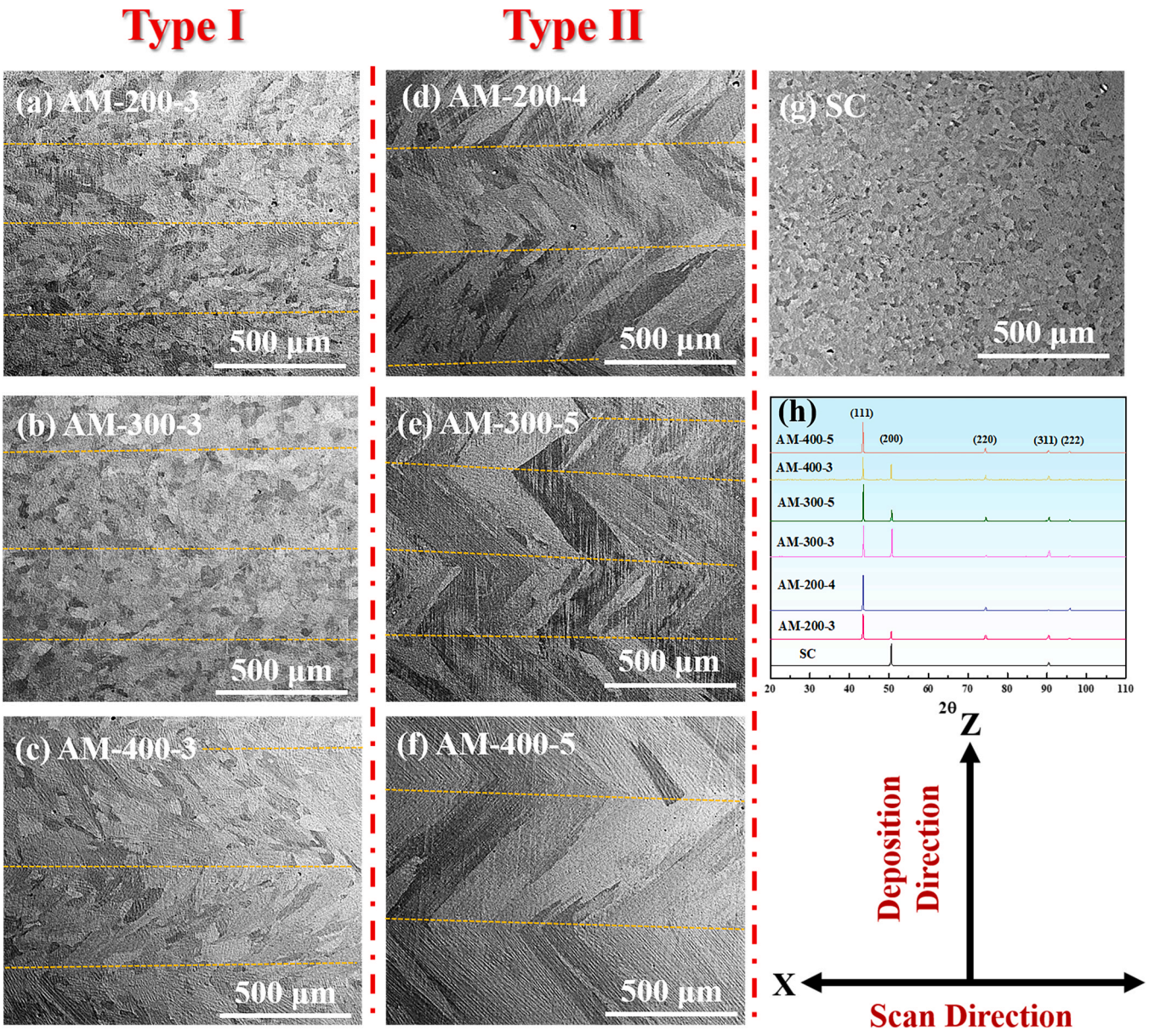

Fig. 2. BSE micrographs of polished FeCoCrNiMn HEAs: (a) AM-200–3; (b) AM-300–3; (c) AM-400–3; (d) AM-200–4; (e) AM-300–5; (f) AM-400–5; (g) SC. The orange lines show the layer boundaries. The deposition and the scanning directions are shown at the bottom right. And the XRD patterns of all samples are shown in (h). (For interpretation of the references to color in this figure legend, the reader is referred to the wed version of this article).

size, and the average secondary dendrite spacing is 8.25 μm. For the equiaxed and cellular dendrites existed in AM-200–3 and AM-200–4, the size of dendrites is finer than that of grains, the average equivalent diameter and cellular arm spacing are 8.31 μm and 4.71 μm, respectively. Fig. 3(g)–(i) shows the detail of the dendrites.

Fig. 4 shows the EBSD maps of SC, AM-200–3 and AM-200–4. The first column shows the inverse pole figure (IPF) maps of SC, AM-200–3, and AM-200–4, where the reference axis is parallel to the scanning direction. The second column shows the grain size distribution histogram, where it can be seen that the two as-built samples have heterogeneous grain size distribution, unlike the SC. The average grain size is obtained from the EBSD data using a conventional mean-linear-intercept method along the tensile axis (parallel to X), and the average grain size of SC, AM-200–3, and AM-200–4 is 30.57 μm, 35.04 μm, and 45.82 μm, respectively. Although there are some abnormal coarse grains in the as-built samples, the average grain size is not much different from that of SC owing to the heterogeneous grain size distribution. The third column in Fig. 4 shows the pole figures of the three samples. It is obvious that SC (max = 3.15 mud—multiples of a uniform density) and AM-200–3 (max = 4.79 mud) have no texture or a weak texture, while AM-200–4 has an obvious texture (max = 16.88 mud), with the < 100 > axis close to 45° with respect to the Z axis. This texture has also been reported in deposited nickel-base superalloys [24].

Fig. 5(a) shows the misorientation distribution histogram obtain from Fig. 4, it can be concluded that the misorientation distribution of SC and AM-200–3 is consistent with the theory, but because of texture, the misorientation distribution of AM-200–4 is deviation from the theory. Moreover, according to the fraction of low-angle (less than 15°) grain boundaries (LAGBs) in the three samples, the order from large to small is as follows: AM-200–4 > AM-200–3 > SC. Fig. 5(d)–(f) are the elemental-distribution maps, and their corresponding grain boundary maps are Fig. 5(g)–(i). It can be found that the equiaxed and cellular dendrites existed in as-built samples produce more LAGBs than columnar dendrites in the SC. In addition, compared with the cellular dendrites grown by epitaxy in AM-200–4, the preferred orientation of equiaxed dendrites in AM-200–3 are not obvious during solidification,

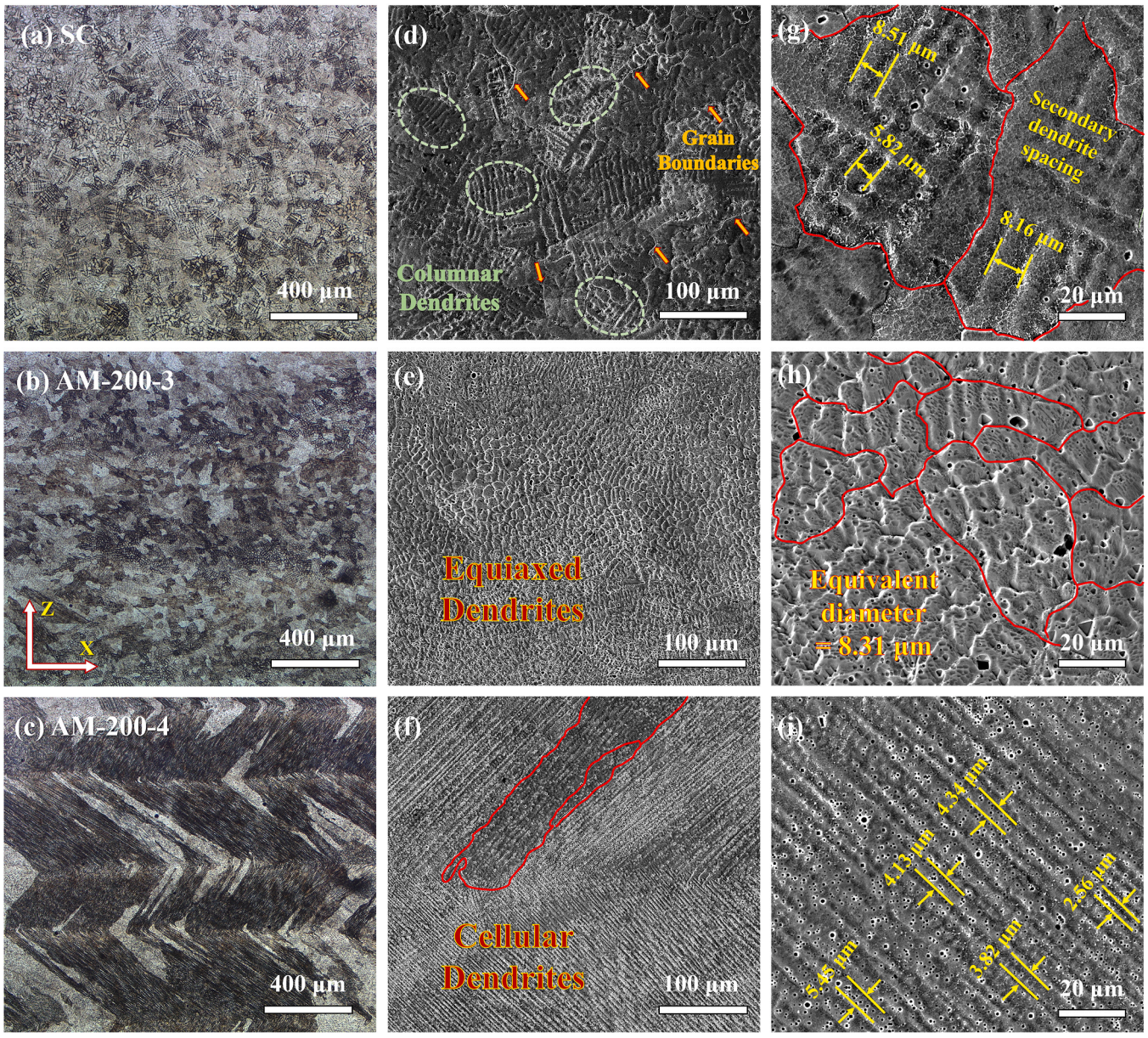

Fig. 3. (a)–(c) are the OM micrographs. (d)–(i) are the SEM micrographs show the solidification structure under large magnification. The first row is the SC sample, the second and third rows are AM-200–3 and AM-200–4, respectively. The green ellipse and yellow arrows, in (c), show the columnar dendrites and grain boundaries, respectively. In (g), (h) and (f), the red lines represent the grain boundaries of three samples. And the measurement of dendrite arm spacing is shown in (g), (h) and (i). (For interpretation of the references to colour in this figure legend, the reader is referred to the web version of this article.)

so it is easy to form larger misorientation than AM-200–4. Therefore, the fraction of LAGBs and the average grain size in AM-200–4 is larger than that of AM-200–3.

Fig. 6(a)–(c) shows the bright TEM field images of SC, AM-200–3, and AM-200–4, the red arrows indicate the grain boundaries. Fig. 6(d)–(f) shows the distribution of dislocations, it can be seen that there are a larger number of dislocations in the two as-built HEAs than that in SC. However, the dislocation cellular structure formed in the other as-built FeCoCrNiMn HEAs and 316 L stainless steel [15,27] is not observed, which is related to the deposition process and deposition strategy adopted in this study. Compared with the SLM process and the bulk deposition strategy, DED process and the single-wall deposition strategy produce lower internal stress and dislocation density, so it is difficult to form dislocation cellular substructures formed by a large number of dislocation tangles, as reported in the literature [28].

3.2. Mechanical properties

Fig. 7 shows the room-temperature tensile properties of FeCoCrNiMn HEAs. Fig. 7(a) presents the engineering stress-strain curves of the HEAs, and combined with Fig. 7(c) and (d), it shows that the yield strength and tensile strength of the six groups as-built samples are higher than those of SC (Yield strength YS = 228 MPa; Ultimate tensile strength UTS = 520 MPa; Uniform elongation ε_u = 45%; Fracture elongation ε_f = 70%), and the uniform elongation of all samples is almost the same, but the fracture elongation of as-built samples is 5–20% less than that of SC, with AM-200–3 exhibiting the best comprehensive mechanical properties (YS = 330 MPa, UTS = 630 MPa, ε_u = 41%, ε_f = 55%). The six as-built samples also have differences in their properties. From Fig. 7 (c) and (d), it can be seen that the yield strength of the materials decreases with increase of laser power (AM-200> AM-300> AM-400), and the scanning speeds at the same power have a small effect on the yield

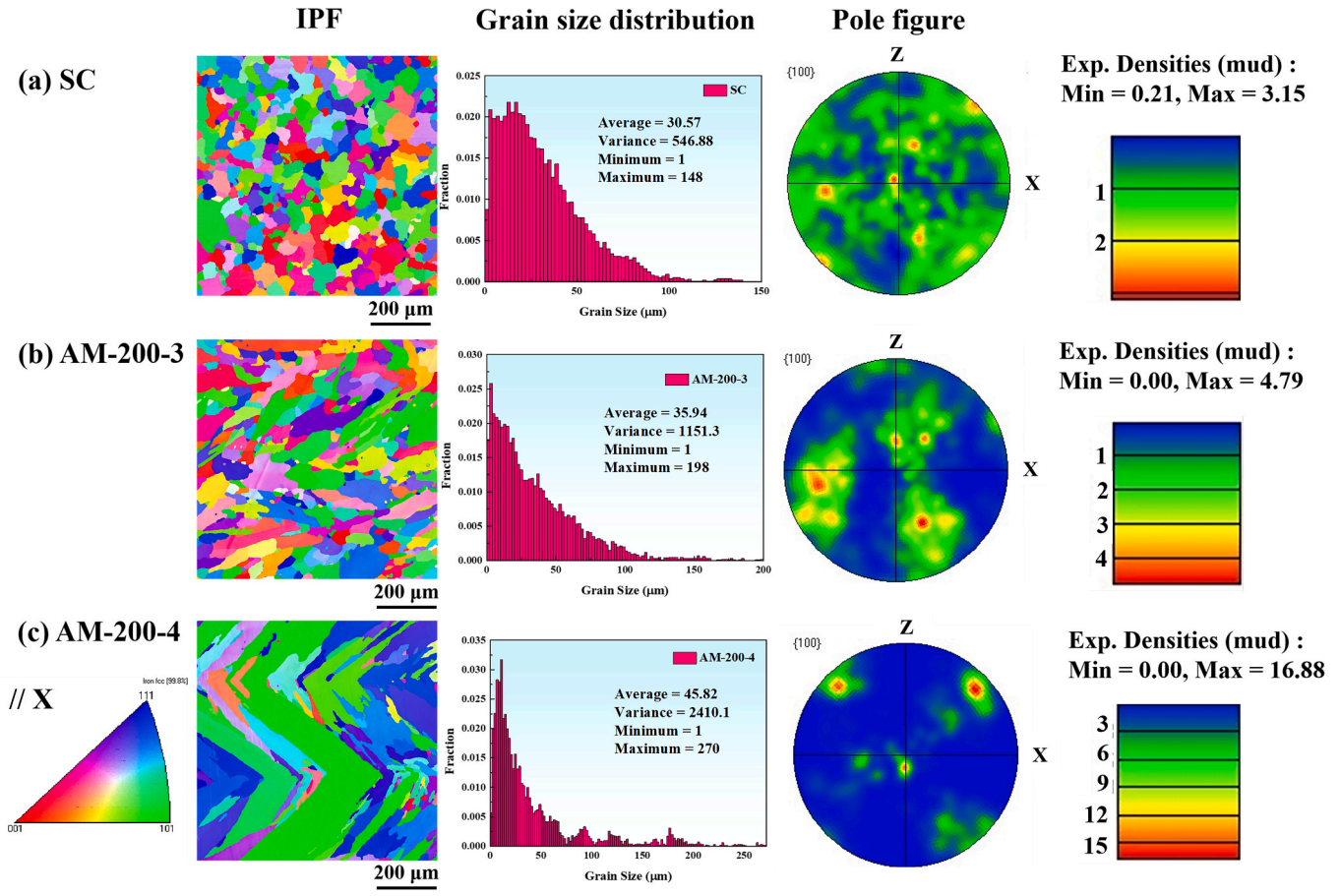

Fig. 4. EBSD maps of the X–Z plane of FeCoCrNiMn HEAs: (a) SC; (b) AM-200–3; (c) AM-200–4. The first column shows IPF maps, with the reference axis is shown at the bottom left, the second column presents grain size distribution histogram, and the third column shows pole figures.

strength, but the ultimate tensile strength of samples with high speeds is lower than that of samples with low speeds. Fig. 7(b) shows the true stress and work hardening rate–true strain curves of SC, AM-200–3 and AM-200–4, where the work hardening behavior of three samples shows typical three-stage characteristics. The work hardening rate of AM-200–3 is higher than that of SC, while AM-200–4 is lower than SC, which leads to the fact that there is no obvious difference in yield strength under the same power for the as-built HEAs, but the ultimate tensile strength decreases with increasing of scanning speed.

3.3. Fracture behavior

Fig. 8 shows the fracture surface and the polished sample surface (X-Z plane) near the fracture. There are dense dimples on the fracture surfaces of SC and as-built samples, which is a characteristic of microporous aggregation fractures. The dimples in the as-built samples are finer than those of SC. In addition, inclusion particles with a size of about 1 μm are found in the fracture surface of the as-built samples, and they are marked with blue circles in Fig. 8(b) and (c). As shown in the inset of Fig. 8(b) and (c), elemental analysis shows that the inclusion is rich in Cr, Mn and O, indicating that the inclusion is an oxide of Mn and Cr formed during the deposition process, and this inclusion is ubiquitous in FeCoCrNiMn HEA [3,15]. It can be seen from the sample surface near the fracture in Fig. 8(d) and (e) that there are many small dense pits on the surface of AM-200–3 in contrast to SC. The pits are correlated with the dimples in the fracture surface, Fig. 8(f), and there are many small particles in these pits. After elemental analysis, it is found that these particles are also Mn and Cr oxides, which indicates that during the deformation process, these oxide inclusions easily become the core of micropore nucleation and deteriorate plasticity.

Fig. 9 shows the tensile sample surface (X–Z plane) of AM-200–3 and AM-200–4 after fracture. It can be found that the sample surface of AM-200–3 is rougher, while the surface of AM-200–4 shows a “Z” shape, which is similar with the grain morphology, as shown in Fig. 9(a) and (b). Many microcracks can be found by magnifying the green boxes in Fig. 9(a) and (b), as shown in Fig. 9(c) and (d). A large number of intergranular cracks are found on the surface of AM-200–3, as shown by the red arrow. The microcracks of AM-200–4 are intragranular cracks, as shown by the yellow arrow. Unlike intergranular cracks, intragranular cracks appear between parallel deformation bands in a grain. The inserts in Fig. 9(c) and (d) show the IPF maps of the sample surface near the fracture, from which it can be found that there is some deformation twinning, which is common in FeCoCrNiMn HEA, and it has been systematically studied [7].

4. Discussion

4.1. Microstructure evolution

There are two-type microstructures of FeCoCrNiMn HEAs fabricated by the DED process, as shown in Fig. 2. The appearance of these two-type microstructures are related to the existence of CET in deposition process [29,30]. As shown in Fig. 10 (a), it shows a schematic diagram of the relationship between dendrite morphology and constitutional supercooling, where G represents the temperature gradient, R denotes the growth speed of solid-liquid interface, and C_0 represents the alloy composition which is constant for the same HEA alloy system. When the C_0 is constant, the smaller the value of G^n/R is, the greater the degree of

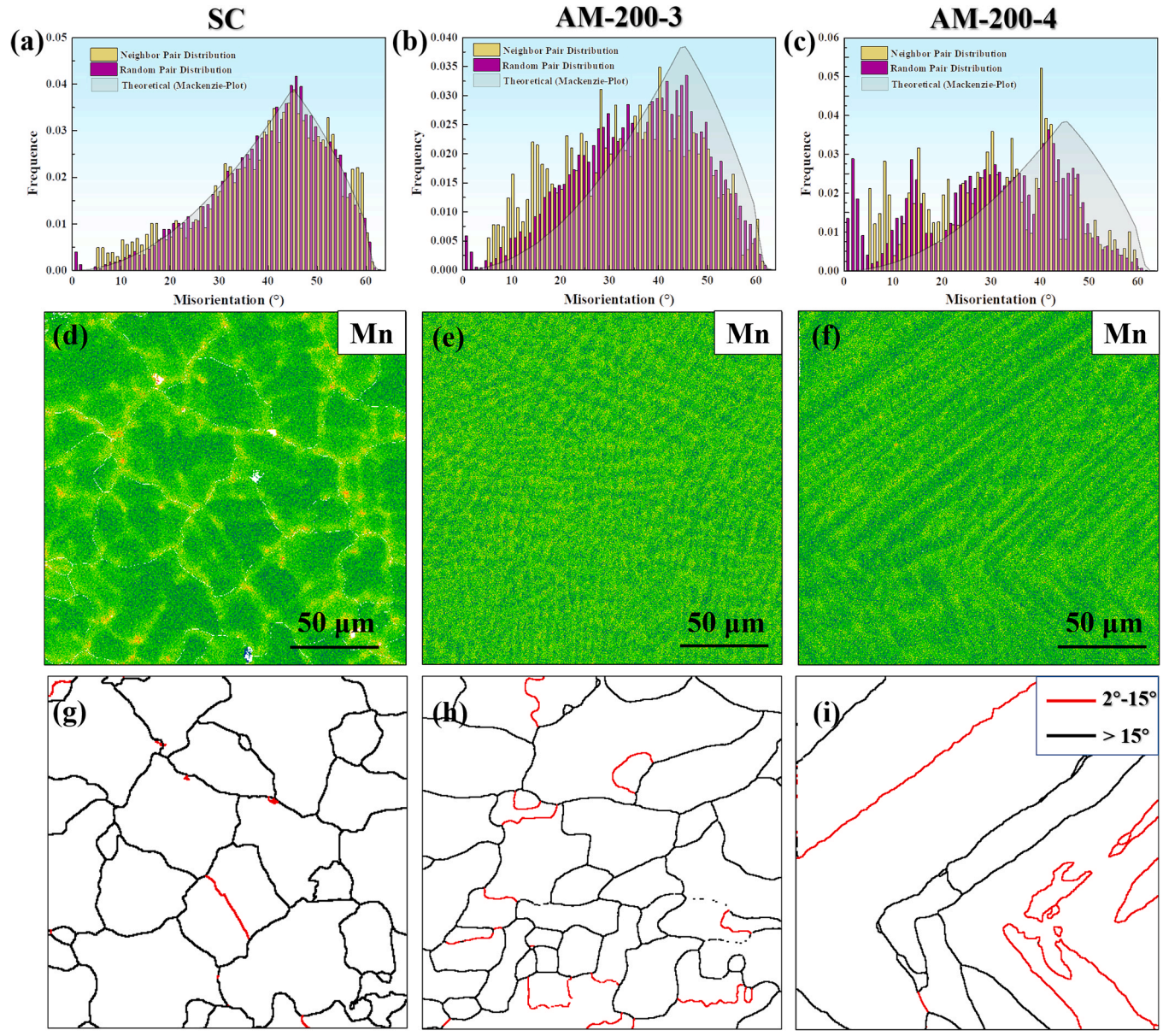

Fig. 5. Misorientation distribution histogram obtained from Fig. 4: (a) SC, (b) AM-200–3 and (C) AM-200–4. Elemental-distribution and grain-boundary maps: (d)–(f) Mn distribution maps of SC, AM-200–3, and AM-200–4; (g)–(i). grain-boundary maps of SC, AM-200–3, and AM-200–4, the red line represents the boundaries between 2° and 5°, and the black line represents the boundaries greater than 15°. (For interpretation of the references to colour in this figure legend, the reader is referred to the web version of this article.)

constitutional supercooling is, and the dendrite morphology will gradually undergo the evolution from columnar to equiaxed.

For the type I, as shown in Fig. S1, equiaxed dendrites are obtained at the top of each layer, while columnar dendrites are obtained at the bottom. As the literature reported [29–32], the temperature gradient G gradually decreases and R increases from the bottom to the top of the molten pool. Therefore, G^n/R gradually decreases from the bottom to the top of the molten pool, the constitutional supercooling increases, and the dendrite morphology changes from columnar to equiaxed. For the type II microstructure, in bidirectional scanning strategy of epitaxial growth, it is necessary to balance the competition between < 100 > -preferential growth direction and the maximum temperature gradient direction [24,25,33]. Consequently, there are two conditions to satisfy: firstly, < 100 > axes are perpendicular to each other in FCC crystal; secondly, the angle between the growth direction of dendrites and the maximum temperature gradient direction in every layer should be consistent. Therefore, the dendrite epitaxial growth mode shown in Fig. 11 will appear, resulting in two < 100 > axes of the crystal being at ±45° with respect to the deposition direction, with one of the < 101 > axes parallel to the scanning direction, forming the texture shown in Fig. 4(c).

Hunt [34] first proposed models to describe the CET phenomenon, which were later modified by Gäumann and Kurz [29]. The relationship between the temperature gradient G and the growth speed R is as follows:

$$G = \frac{1}{n+1}\cdot\sqrt[3]{\frac{-4\pi N_0}{3\ln(1-\varphi)}}\cdot\left(1-\frac{\Delta T_n^{n+1}}{(a\cdot R)^{n+1/n}}\right)\cdot(a\cdot R)^{1/n}, \quad (2)$$

where G is the temperature gradient (K/m), R is the solidification speed (m/s), n and a are material dependent constants, N_0 is the density of nuclei ($/m^3$), φ is the volume fraction of the equiaxed grains, and ΔT_n is

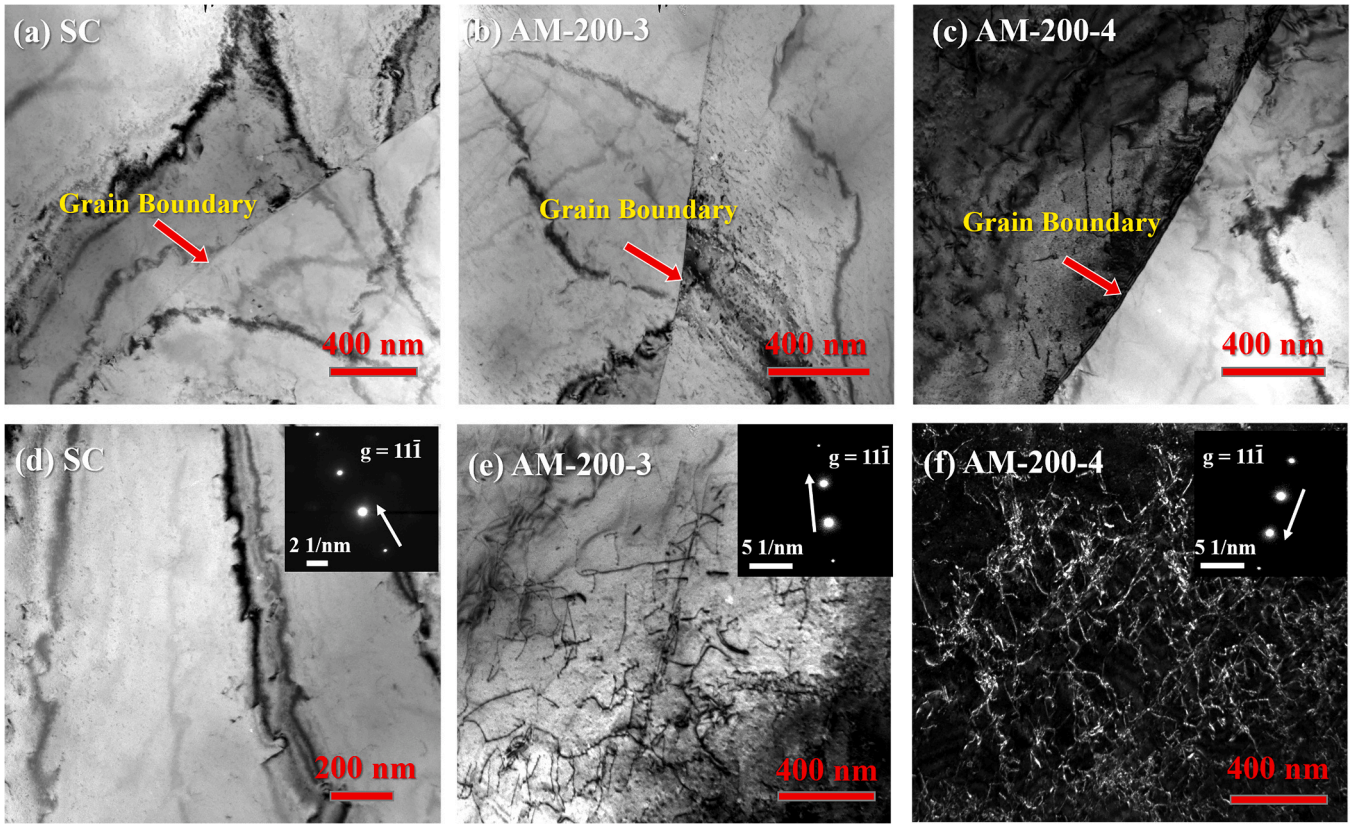

Fig. 6. Bright TEM field image: (a) SC; (b) AM-200–3; (c) AM-200–4. The red arrows indicate grain boundary; (d), (e) and (f) show the distribution of dislocations existed in SC, AM-200–3 and AM-200–4. (For interpretation of the references to colour in this figure legend, the reader is referred to the web version of this article.)

the nucleation undercooling.

Based on Eq. (2), a microstructure selection map for FeCoCrNiMn HEA is proposed, as shown in Fig. 10 (b). The parameters are obtained from the literatures [29,35,36], where $a = 1.25 \times 10^3$ $K^{3.4}$·s/mm, $n = 3.4$ and $\Delta T_n = 2.5$ °C. And from the works of Guan et al. [20,36], when the G is 207 K/mm, R is 5 mm/s, the columnar grains are obtained, thus, the $N_0 \leq 5.6 \times 10^4$ /mm^3, here $N_0 = 5.6 \times 10^4$ /mm^3 is adopted.

In laser deposition processes, the increase of scanning speed will simultaneously increase the solidification speed R and temperature gradient G, which will lead to two conditions for microstructure evolution, as situation 1 (S1) and situation 2 (S2) shown in Fig. 10 (b). For S1, the typical alloy is Ti-6Al-4 V, as reported by Ren et al. [21], although the range of G and R of Ti-6Al-4 V is different from that shown in Fig. 10 (b). Their results show that the width of the prior-β grains decreased from 1000 μm to 630 μm with the increase of scanning speed, but the microstructure is still the mixed. Contrastively, with the increase of scanning speed, FeCoCrNiMn HEA is easy to make the solidification region fall in the columnar-grain-growth region, as shown by the orange arrow S2 in Fig. 10 (b), which indicates scanning speed has a greater impact on G than R. Because of the near-equiatomic ratios of the composition, the CET behavior of the HEAs is different from the traditional alloys. Therefore, the constitutional supercooling theory and the microstructure selection maps for HEAs need to be further studied to guide the selection of composition and process parameters of additively manufactured HEAs.

4.2. Strengthening mechanisms

FeCoCrNiMn HEAs fabricated by DED have good comprehensive mechanical properties. In the literature, the strengthening mechanisms of FeCoCrNiMn HEA are: grain boundary strengthening [37], dislocation strengthening [15], second-phase strengthening [10,16] and twinning strengthening [3]. It can be seen from Section 3.1 that the HEAs obtained in this work is a single-phase FCC structure. Although Mn and Cr rich oxides have been found at the fracture surface, and Kim et al. [16] have also studied strength improvement caused by nanoscale oxide particles, the size of the oxide obtained here reaches the micron level, which cannot play the role of second-phase strengthening, but can only deteriorate plasticity [3,14,15]. At the room-temperature tensile test, the deformation twinning appears in the late stage of tensile test for FeCoCrNiMn alloys [6], so it has no effect on yield strength. It can be seen from Fig. 6 that there are many dislocations in the as-built samples. Therefore, a quantitative calculation is carried out for grain boundary strengthening ($\Delta\sigma_G$) and dislocation strengthening ($\Delta\sigma_D$).

For grain boundary strengthening, the classic Hall–Petch equation is used, as shown in Eq. (3). The grain size d is obtained from Section 3.1. Through quantitative calculations, the strength of SC, AM-200–3, and AM-200–4 after grain boundary strengthening is: 214.3 MPa, 207.4 MPa, and 198.0 MPa, respectively.

$$\sigma_s = \sigma_0 + k \times d^{-\frac{1}{2}}, \tag{3}$$

where σ_0 = 125 MPa, k = 494 MPa·$\mu m^{1/2}$ [8], d is the average grain size.

The dislocation density can be obtained from the WH method through Eqs. (4) and (5) [38], $\rho_{AM\text{-}200\text{-}3} = 5.01 \times 10^{13}$ m^{-2}, and $\rho_{AM\text{-}200\text{-}4} = 4.05 \times 10^{13}$ m^{-2}. The dislocation strengthening term is calculated using Eq. (6), where M is the Taylor factor, which is closely related to the grain orientation, so the average value of M can be calculated from the EBSD data. The theoretical yield strength of the two as-built samples after adding the dislocation strengthening term are 299.2 MPa and 284.5 MPa.

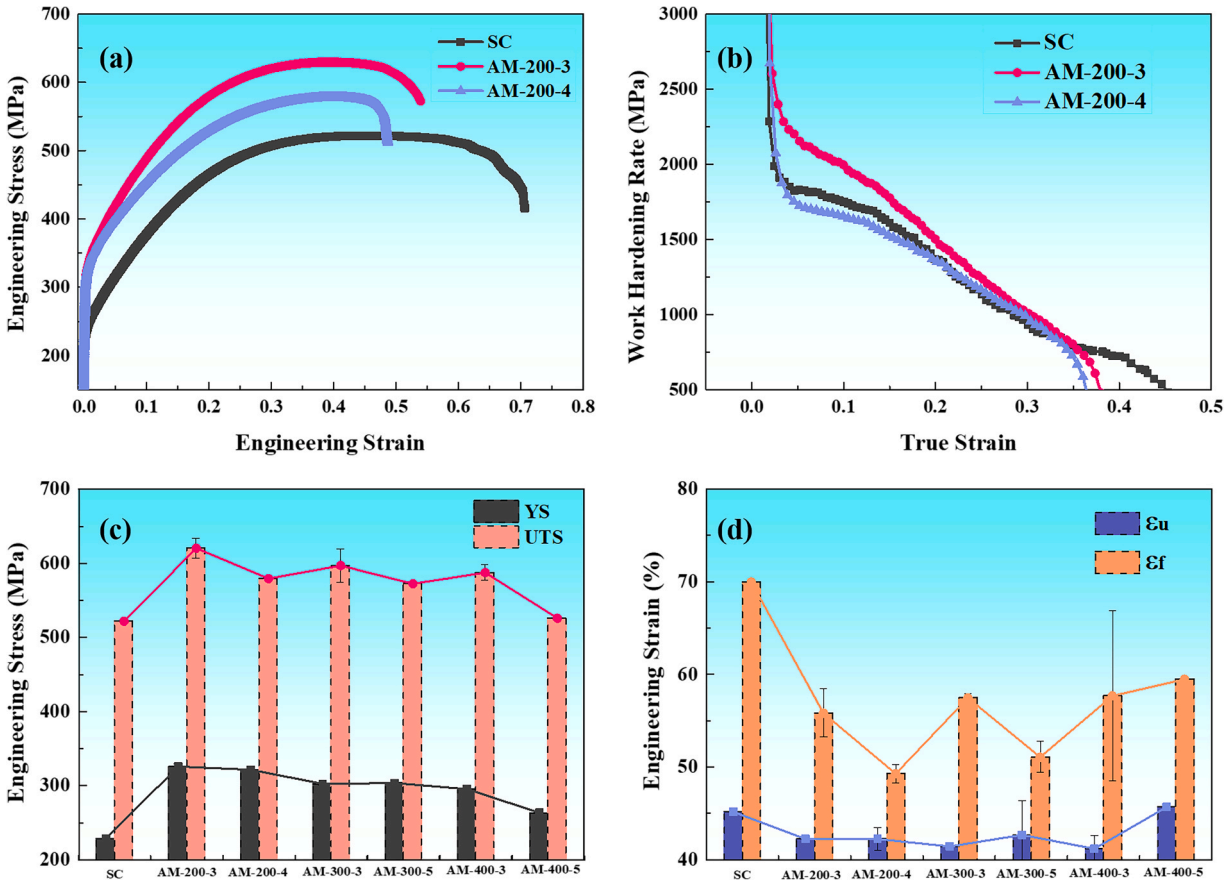

Fig. 7. Room-temperature mechanical properties of FeCoCrNiMn HEAs: (a) engineering stress–strain curves; (b) true stress and work hardening rate *versus* true strain curves; (c) histogram of yield strength (YS) and ultimate tensile strength (UTS); (d) histogram of uniform elongation (ε_u) and total elongation (ε_f) .

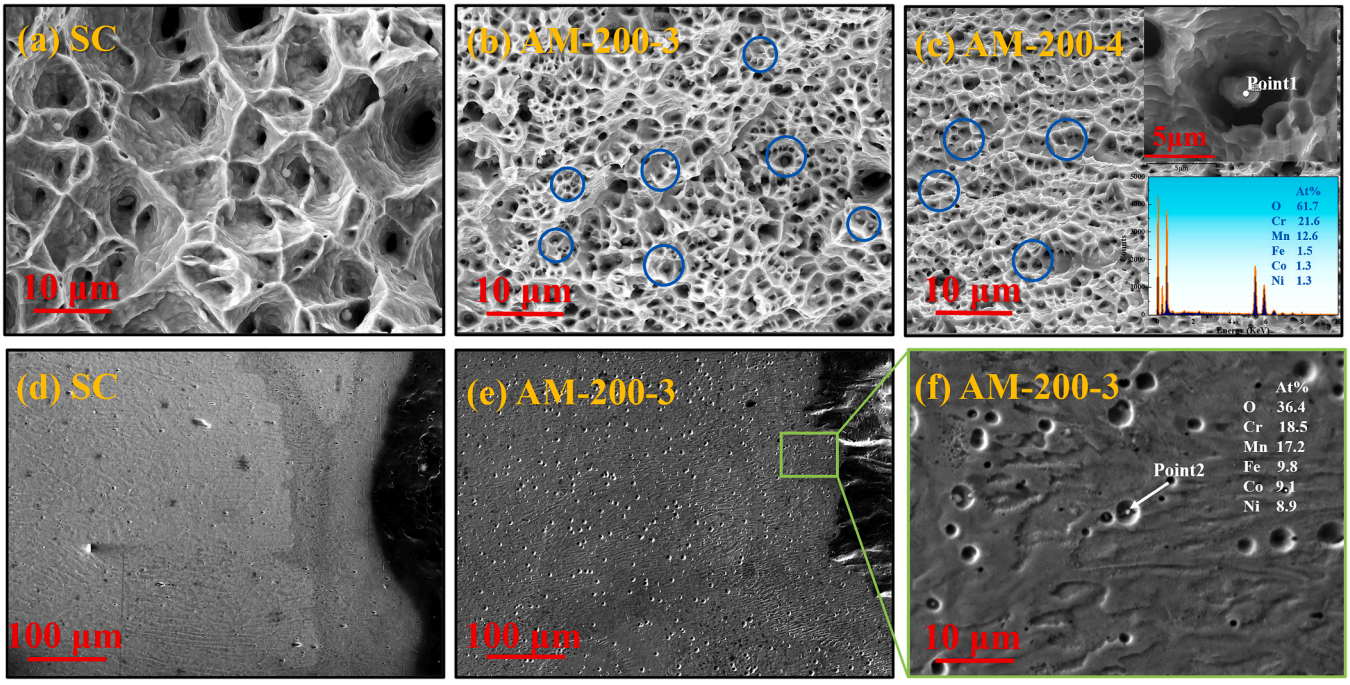

Fig. 8. (a), (b) and (c) show the fracture surface of SC, AM-200–3 and AM-200–4, respectively. The insert in (c) shows a magnification graph and EDS map of the inclusions. (d) and (e) show the polished tensile sample surface (X–Z plane) near the fracture of SC and AM-200–3; (f) is the magnification graph of the green box in (e), and the inset in (f) is the composition of point 2. (For interpretation of the references to colour in this figure legend, the reader is referred to the web version of this article.)

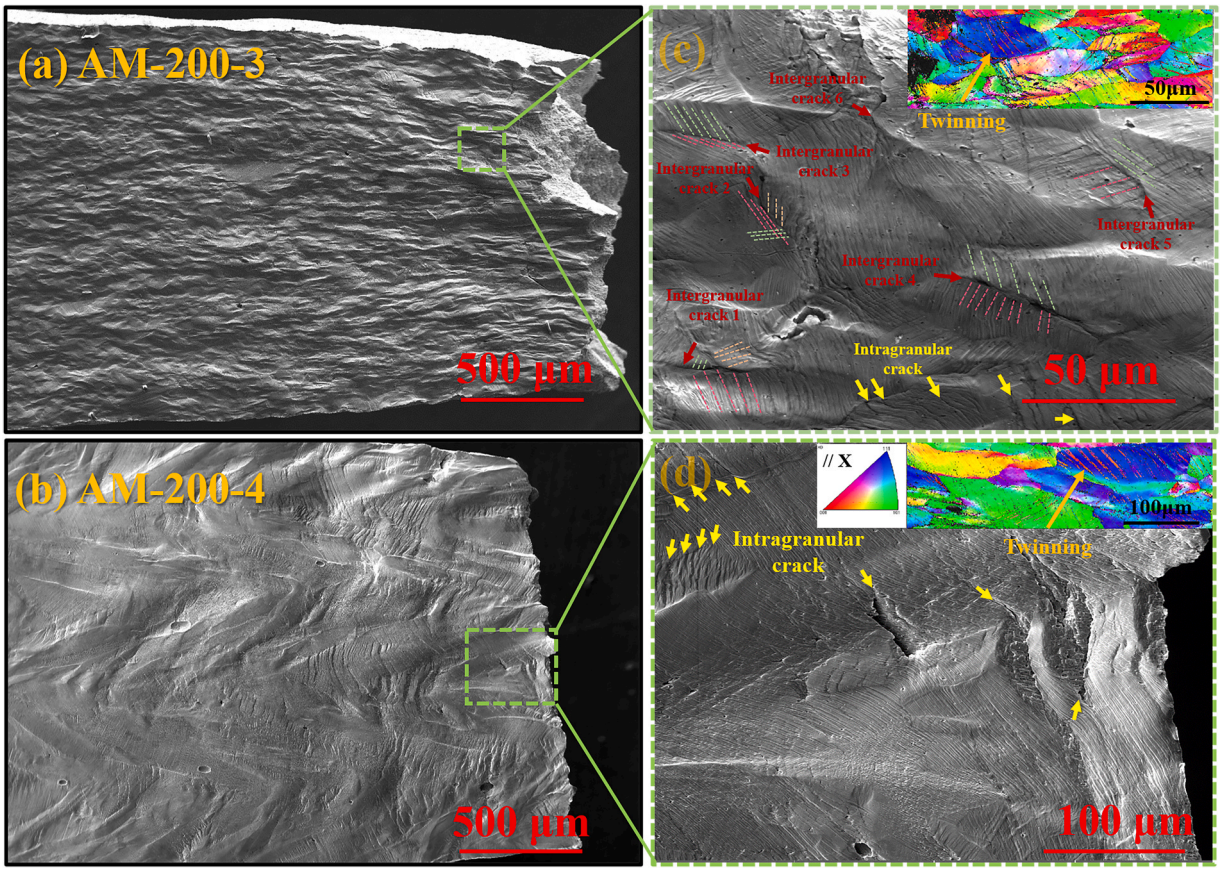

Fig. 9. The characteristics of microcracks: (a) and (b) show the tensile sample surface of AM-200–3 and AM-200–4 after fracture, respectively; (c) and (d) present the magnification view of the green box in (a) and (b), respectively, and the inserts are EBSD images of the sample surface near the fracture. The dotted lines in (c) represent different slip or twinning traces, the red and yellow arrows represent intergranular and intragranular cracks, respectively. (For interpretation of the references to colour in this figure legend, the reader is referred to the web version of this article.)

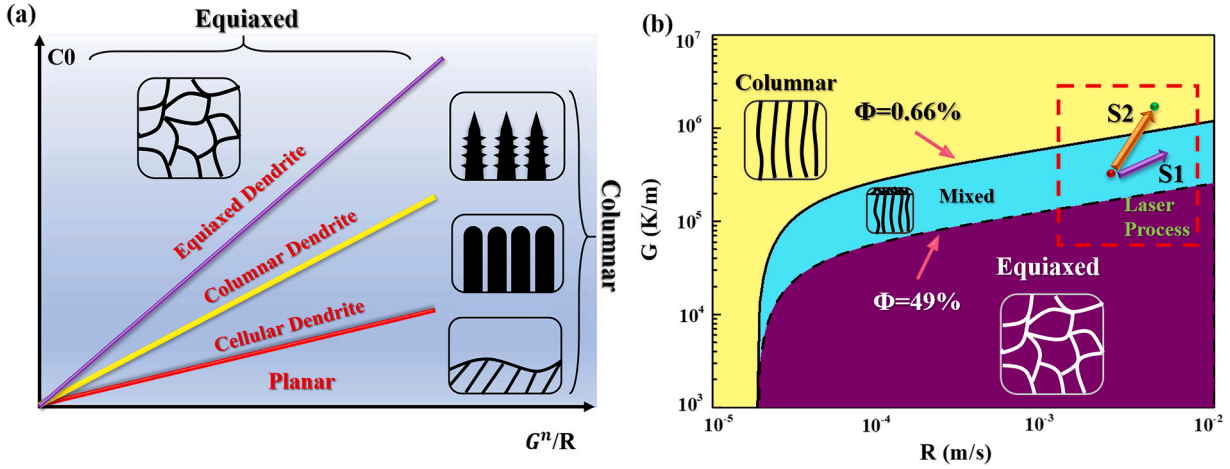

Fig. 10. (a) Schematic diagram of the relationship between dendritic morphology and constitutional supercooling (G^n/R); (b) a microstructure selection map for FeCoCrNiMn high-entropy alloy, where the red box shows the range of conditions that are typical for the laser process. When G and R increase simultaneously, there will be two conditions for the evolution of the microstructure, as shown by S1 and S2. The red and green dots in (b) represent the low and high-speed conditions, respectively, for FeCoCrNiMn HEAs at the same power. (For interpretation of the references to colour in this figure legend, the reader is referred to the web version of this article.)

$$\beta cos\theta = \frac{K\lambda}{D} + (4sin\theta)\cdot\varepsilon, \tag{4}$$

$$\rho = 2\sqrt{3}\cdot\varepsilon \Big/ (Db), \tag{5}$$

where β is the FWHM; θ is the Bragg angle of a certain peak; $\lambda = 0.15405$ nm is the wavelength of Cu Kα radiation; K = 0.9 is a constant; and D is the crystallite size.

$$\Delta\sigma_D = M\alpha Gb\rho^{1/2}, \tag{6}$$

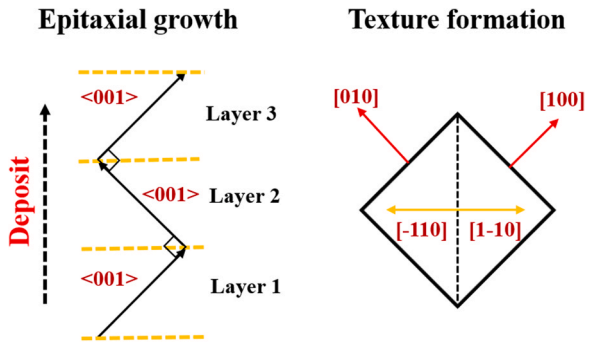

Fig. 11. Schematic diagram of epitaxial growth and the formation of texture of type II microstructure.

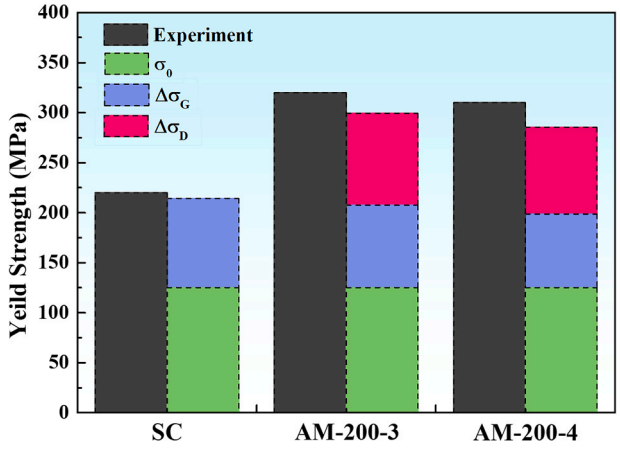

Fig. 12. The strength contributions of different mechanisms and comparison between the experimental (left) and calculations (right) results.

where M is the Taylor factor, which can be calculated from the EBSD data, $M_{SC} = 3.02$, $M_{AM\text{-}200\text{-}3} = 3.20$, $M_{AM\text{-}200\text{-}4} = 3.35$; $\alpha = 0.2$ is a constant for FCC metals; $G = 80$ GPa is the shear modulus; $b = 0.2536$ nm is the Burgers vector of the full dislocation.

The comparison between theory and experiment is shown in Fig. 12. It can be found that the theoretical value of SC is in agreement with the experiment, but the theoretical yield strength of as-built samples is about 30 MPa lower than the experiment results. As the literature reported [39], the simple Hall–Petch relationship is not suitable for as-built AM materials with complex topology and heterogeneous distribution grains, it was found that the Hall-Petch coefficient of AM 316 L stainless steel have significant variability compared with the wrought samples. This may be the reason for the difference between theory and experiment yield strength of as-built samples. Moreover, it can be concluded from Fig. 12 that dislocation strengthening also plays an important role in improving the yield strength for the AM FeCoCrNiMn HEAs.

4.3. Work hardening behavior

The AM-200–3 and AM-200–4 have different initial work hardening rate when their dislocation densities are not significantly different. Moreover, in single-phase solid-solution HEAs fabricated by traditional process, the smaller the grain size is, the lower the work hardening rate is [40,41], which is contrary to our results. According to Section 3.1, because of the texture formation during deposition, the main differences in microstructure of the two samples are as follows: (1) AM-200–4 has the texture of $< 110 >$ // tensile axis; (2) the average misorientation of AM-200–3 is larger than that of AM-200–4. And from Section 3.3, the two as-built samples show different characteristics of microcracks. To investigate the formation of microcracks, *in-situ* HR-DIC experiment was carried out on AM-200–3 which has the intergranular and intragranular cracks.

From Fig. 13 (a) and (b), the strain distribution maps under strains of 3.5% and 7.5%, it can be found that the strain distribution is heterogeneous, and the strain is concentrated in two regions: one is the slip band region, which is parallel to the slip trace; the other is the intersection zone of the slip traces with different orientations, as shown by the black circles, and their corresponding positions in Fig. 13 (c) are marked with yellow arrows. Fig. 13 (d) and (e) show the BSE and strain distribution maps when the strain is 35%. It can be seen that the intragranular cracks appear in the first kind strain concentrated regions, as shown by the yellow arrows; and the intergranular cracks appear in the region 1 and 2 of Fig. 13 (a), as shown by the red arrows. These two-type microcracks correspond to two different deformation behaviors of AM-200–3 and AM-200–4, that is, the role of grain boundary in AM-200–3 is more important than that in AM-200–4.

As we all know, the grain boundaries can impede the motion of dislocations, known as grain-boundary strengthening. Actually, different grain boundaries have different effects on dislocations. Abuzaid et al. [42,43] use the residual Burgers vectors to describe the resistance of slip transmission at the grain boundaries. The result shows a higher energy barrier for slip transmission a higher magnitudes of the residual Burgers vector. However, the relationship between residual Burgers vector and the characteristics of grain boundary (misorientation, rotation axis, normal direction) is not clear, and in this work, AM-200–3 with larger grain boundary misorientation shows obvious characteristics of intergranular cracks. Therefore, it is necessary to further study the effect of different grain boundaries on dislocations.

In addition, it can be seen from Fig. 13 (e) that there are obvious deformation differences between the two grains. Through the IPF figure at this region, Fig. 13 (f), it can be seen that the orientation of grain 2 with large strain is close to $< 110 >$ // tensile axis, and the grain 1 with small strain is close to $< 111 >$ // tensile axis, that is, under the same stress, the grains with $< 110 >$ orientation produce larger strain than $< 111 >$, so the work hardening rate will be reduced. The results of FCC HEAs single crystal tensile experiments [44–46] also show that the samples with $< 111 >$ orientation are more likely to active deformation twinning and twin-twin interactions to obtain higher work hardening rate, while the samples with $< 110 >$ orientation or close to $< 110 >$, for example $< 144 >$, are dominated by dislocation slip at the initial stage of deformation, and deformation twinning will not appear until the later stage of deformation. Therefore, $< 110 >$ texture is also one of the main reasons for the low work hardening rate of AM-200–4, on the other hand, in the additive manufacturing process, changing the texture component of the sample by adjusting the process parameters is also an important way to adjust the material properties.

5. Conclusion

FeCoCrNiMn HEAs were successfully fabricated by DED process. By comparing with the suction-casting HEAs, the influence of CET on the microstructure and mechanical properties of as-built FeCoCrNiMn HEAs were studied, providing the necessary basis for the future development of additively manufactured HEAs. The main conclusions are as follows:

1. At the same laser power, the temperature gradient G and the solidification speed R of the molten pool increase with the scanning speed, but its influence on the temperature gradient is greater, this results in the decrease of constitutional supercooling, changes the solidification structure from the mix of equiaxed and columnar dendrites at low speed to cellular dendrites at high speed, and modifies the microstructure from near fully equiaxed grains to columnar grains with obvious texture and “Zigzag” epitaxial growth.

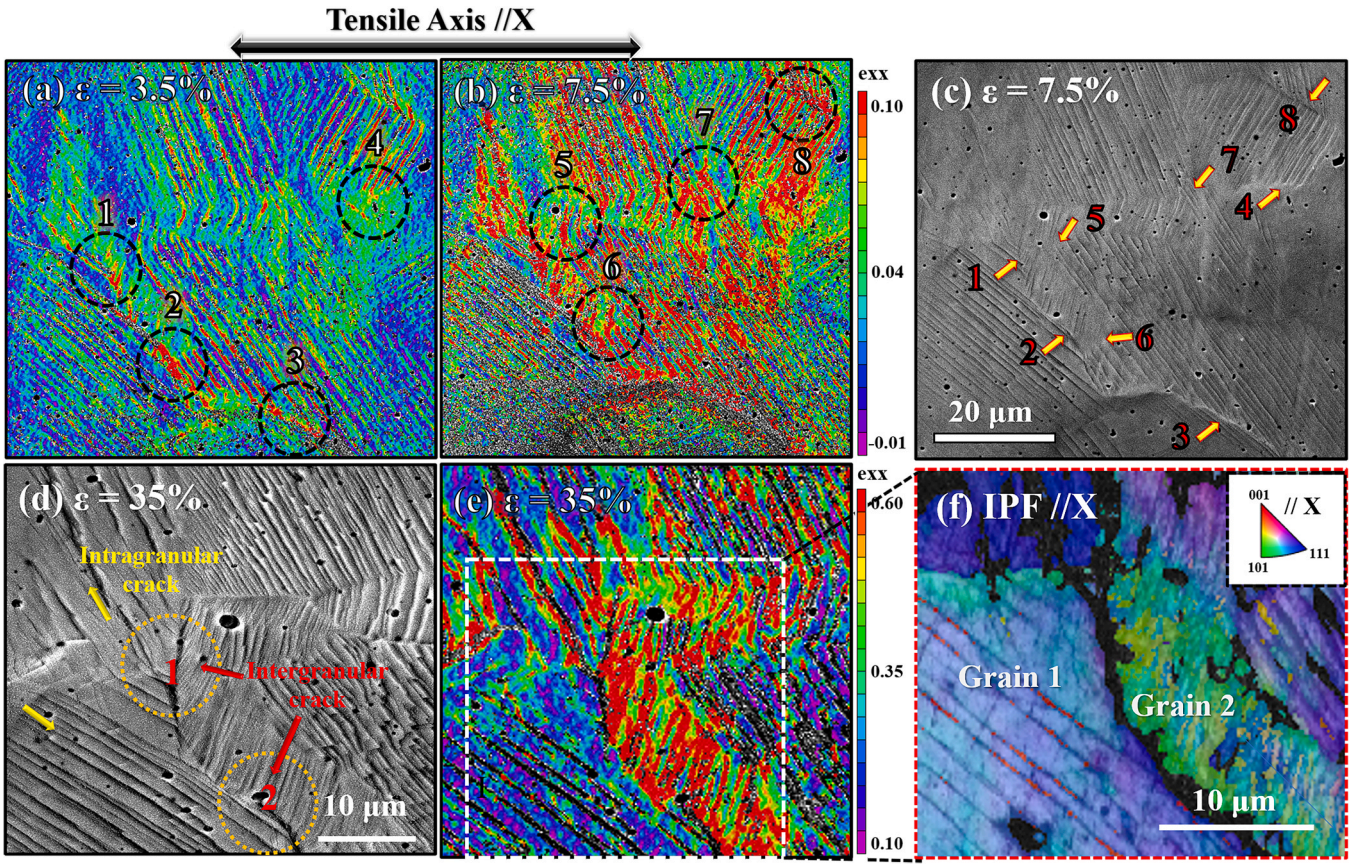

Fig. 13. (a), (b) and (e) are the HR-DIC strain distribution maps under different engineering strains: 3.5%, 7.5% and 35%, respectively. (c) and (d) are the BSE maps of (b) and (e), respectively. (f) is the EBSD map of the white box in (e). The black dash circles in (a) and (b) represent 8 strain concentrated regions which correspond to those indicated by the yellow arrows in (c). The red and yellow arrows in (d) represent intergranular and intragranular cracks, respectively, and the orange circles correspond to the region 1 and region2 in (c). (For interpretation of the references to colour in this figure legend, the reader is referred to the web version of this article.)

2. Comparing with conventional materials, the two-kind as-built FeCoCrNiMn HEAs have complex and heterogeneous microstructures. The unique features of as-built HEAs include layer boundaries, heterogeneous grain-size distribution, texture, small dendrite substructure, LAGBs, high dislocation density, and a large number of Mn-Cr rich oxide inclusions.
3. The room-temperature strength of as-built HEAs is increased by about 100 MPa compared with SC, with AM-200–3 having the best comprehensive mechanical properties (YS = 330 MPa, UTS = 630 MPa, εu = 41%, εf = 55%). Through quantitative calculations, it is found that the strength of as-built samples can be improved mainly by dislocation strengthening and grain boundary strengthening, and the Mn-Cr rich oxide inclusions can be the core of micropore nucleation and deteriorate plasticity.
4. The work hardening rate of equiaxed structure without texture is higher than that of columnar structure with texture (< 110 > // tensile axis). There are two main reasons: firstly, because of the texture, the grain boundaries play a more important role in the deformation behavior of equiaxed structure than that in columnar structure, which makes the microcracks of equiaxed structure mostly are intergranular cracks, whereas, the columnar structure shows the characteristics of intragranular cracks; secondly, the deformation behavior of columnar structure is dominated by the grain orientation, and the < 110 > orientation will reduce the work hardening rate.

CRediT authorship contribution statement

Mengyao Zheng: Investigation, Data curation, Writing- original draft preparation; **Chuanwei Li**: Conceptualization, Methodology, Supervision; **Xinyu Zhang**: Investigation, Data curation; **Zhenhua Ye**: Formal analysis, Software; **Xudong Yang**: Investigation, Validation; **Jianfeng Gu**: Supervision, Writing - reviewing & editing.

Declaration of Competing Interest

The authors declare that they have no known competing financial interests or personal relationships that could have appeared to influence the work reported in this paper.

Acknowledgments

This work was supported by the National Natural Science Foundation of China (Grant No. 51971145, No. 51801126) and the National Key Research and Development Program of China (Grant No. 2018YFA0702905).

Appendix A. Supporting information

Supplementary data associated with this article can be found in the online version at doi:10.1016/j.addma.2020.101660.

References

[1] J.W. Yeh, S.K. Chen, S.J. Lin, J.Y. Gan, T.S. Chin, T.T. Shun, C.H. Tsau, S.Y. Chang, Nanostructured high-entropy alloys with multiple principal elements: novel alloy design concepts and outcomes, Adv. Eng. Mater. 6 (2004) 299–303, https://doi.org/10.1002/adem.200300567.

[2] B. Cantor, I.T.H. Chang, P. Knight, A.J.B. Vincent, Microstructural development in equiatomic multicomponent alloys, Mater. Sci. Eng. A 375–377 (2004) 213–218, https://doi.org/10.1016/j.msea.2003.10.257.

[3] B. Gludovatz, A. Hohenwarter, D. Catoor, E.H. Chang, E.P. George, R.O. Ritchie, A fracture-resistant high-entropy alloy for cryogenic applications, Science 80 (345) (2014) 1153–1158, https://doi.org/10.1126/science.1254581.

[4] T. Yang, Y.L. Zhao, Y. Tong, Z.B. Jiao, J. Wei, J.X. Cai, X.D. Han, D. Chen, A. Hu, J. J. Kai, K. Lu, Y. Liu, C.T. Liu, Multicomponent intermetallic nanoparticles and superb mechanical behaviors of complex alloys, Science 80 (362) (2018) 933–937, https://doi.org/10.1126/science.aas8815.

[5] Z. Li, K.G. Pradeep, Y. Deng, D. Raabe, C.C. Tasan, Metastable high-entropy dual-phase alloys overcome the strength-ductility trade-off, Nature 534 (2016) 227–230, https://doi.org/10.1038/nature17981.

[6] M. Naeem, H. He, F. Zhang, H. Huang, S. Harjo, T. Kawasaki, B. Wang, S. Lan, Z. Wu, F. Wang, Y. Wu, Z. Lu, Z. Zhang, C.T. Liu, X.L. Wang, Cooperative deformation in high-entropy alloys at ultralow temperatures, Sci. Adv. 6 (2020), https://doi.org/10.1126/sciadv.aax4002.

[7] G. Laplanche, A. Kostka, O.M. Horst, G. Eggeler, E.P. George, Microstructure evolution and critical stress for twinning in the CrMnFeCoNi high-entropy alloy, Acta Mater. 118 (2016) 152–163, https://doi.org/10.1016/j.actamat.2016.07.038.

[8] F. Otto, A. Dlouhý, C. Somsen, H. Bei, G. Eggeler, E.P. George, The influences of temperature and microstructure on the tensile properties of a CoCrFeMnNi high-entropy alloy, Acta Mater. 61 (2013) 5743–5755, https://doi.org/10.1016/j.actamat.2013.06.018.

[9] E.J. Pickering, R. Muñoz-Moreno, H.J. Stone, N.G. Jones, Precipitation in the equiatomic high-entropy alloy CrMnFeCoNi, Scr. Mater. 113 (2016) 106–109, https://doi.org/10.1016/j.scriptamat.2015.10.025.

[10] M.V. Klimova, D.G. Shaysultanov, S.V. Zherebtsov, N.D. Stepanov, Effect of second phase particles on mechanical properties and grain growth in a CoCrFeMnNi high entropy alloy, Mater. Sci. Eng. A 748 (2019) 228–235, https://doi.org/10.1016/j.msea.2019.01.112.

[11] S. Gorsse, C. Hutchinson, M. Gouné, R. Banerjee, Additive manufacturing of metals: a brief review of the characteristic microstructures and properties of steels, Ti-6Al-4V and high-entropy alloys, Sci. Technol. Adv. Mater. 18 (2017) 584–610, https://doi.org/10.1080/14686996.2017.1361305.

[12] D.D. Gu, W. Meiners, K. Wissenbach, R. Poprawe, Laser additive manufacturing of metallic components: materials, processes and mechanisms, Int. Mater. Rev. 57 (2012) 133–164, https://doi.org/10.1179/1743280411Y.0000000014.

[13] T. Borkar, B. Gwalani, D. Choudhuri, C.V. Mikler, C.J. Yannetta, X. Chen, R. V. Ramanujan, M.J. Styles, M.A. Gibson, R. Banerjee, A combinatorial assessment of AlxCrCuFeNi2 ($0 < x < 1.5$) complex concentrated alloys: microstructure, microhardness, and magnetic properties, Acta Mater. 116 (2016) 63–76, https://doi.org/10.1016/j.actamat.2016.06.025.

[14] Y. Chew, G.J. Bi, Z.G. Zhu, F.L. Ng, F. Weng, S.B. Liu, S.M.L. Nai, B.Y. Lee, Microstructure and enhanced strength of laser aided additive manufactured CoCrFeNiMn high entropy alloy, Mater. Sci. Eng. A 744 (2019) 137–144, https://doi.org/10.1016/j.msea.2018.12.005.

[15] Z.G. Zhu, Q.B. Nguyen, F.L. Ng, X.H. An, X.Z. Liao, P.K. Liaw, S.M.L. Nai, J. Wei, Hierarchical microstructure and strengthening mechanisms of a CoCrFeNiMn high entropy alloy additively manufactured by selective laser melting, Scr. Mater. 154 (2018) 20–24, https://doi.org/10.1016/j.scriptamat.2018.05.015.

[16] Y.K. Kim, J. Choe, K.A. Lee, Selective laser melted equiatomic CoCrFeMnNi high-entropy alloy: microstructure, anisotropic mechanical response, and multiple strengthening mechanism, J. Alloy. Compd. 805 (2019) 680–691, https://doi.org/10.1016/j.jallcom.2019.07.106.

[17] F. Weng, Y. Chew, Z. Zhu, X. Yao, L. Wang, F.L. Ng, S. Liu, G. Bi, Excellent combination of strength and ductility of CoCrNi medium entropy alloy fabricated by laser aided additive manufacturing, Addit. Manuf. 34 (2020), 101202, https://doi.org/10.1016/j.addma.2020.101202.

[18] N. Kashaev, V. Ventzke, N. Stepanov, D. Shaysultanov, V. Sanin, S. Zherebtsov, Laser beam welding of a CoCrFeNiMn-type high entropy alloy produced by self-propagating high-temperature synthesis, Intermetallics 96 (2018) 63–71, https://doi.org/10.1016/j.intermet.2018.02.014.

[19] M.A. Melia, J.D. Carroll, S.R. Whetten, S.N. Esmaeely, J. Locke, E. White, I. Anderson, M. Chandross, J.R. Michael, N. Argibay, E.J. Schindelholz, A.B. Kustas, Mechanical and corrosion properties of additively manufactured CoCrFeMnNi high entropy alloy, Addit. Manuf. 29 (2019), 100833, https://doi.org/10.1016/j.addma.2019.100833.

[20] S. Guan, D. Wan, K. Solberg, F. Berto, T. Welo, T.M. Yue, K.C. Chan, Additive manufacturing of fine-grained and dislocation-populated CrMnFeCoNi high entropy alloy by laser engineered net shaping, Mater. Sci. Eng. A 761 (2019), 138056, https://doi.org/10.1016/j.msea.2019.138056.

[21] Y.M. Ren, X. Lin, X. Fu, H. Tan, J. Chen, W.D. Huang, Microstructure and deformation behavior of Ti-6Al-4V alloy by high-power laser solid forming, Acta Mater. 132 (2017) 82–95, https://doi.org/10.1016/j.actamat.2017.04.026.

[22] J.J. Blecher, T.A. Palmer, T. Debroy, Solidification map of a nickel-base alloy, Metall. Mater. Trans. A Phys. Metall. Mater. Sci. 45 (2014) 2142–2151, https://doi.org/10.1007/s11661-013-2149-1.

[23] F. Di Gioacchino, J. Quinta da Fonseca, Plastic strain mapping with sub-micron resolution using digital image correlation, Exp. Mech. 53 (2013) 743–754, https://doi.org/10.1007/s11340-012-9685-2.

[24] G.P. Dinda, A.K. Dasgupta, J. Mazumder, Texture control during laser deposition of nickel-based superalloy, Scr. Mater. 67 (2012) 503–506, https://doi.org/10.1016/j.scriptamat.2012.06.014.

[25] H.L. Wei, J. Mazumder, T. DebRoy, Evolution of solidification texture during additive manufacturing, Sci. Rep. 5 (2015) 1–7, https://doi.org/10.1038/srep16446.

[26] A. Yadollahi, N. Shamsaei, S.M. Thompson, D.W. Seely, Effects of process time interval and heat treatment on the mechanical and microstructural properties of direct laser deposited 316L stainless steel, Mater. Sci. Eng. A 644 (2015) 171–183, https://doi.org/10.1016/j.msea.2015.07.056.

[27] Y.M. Wang, T. Voisin, J.T. McKeown, J. Ye, N.P. Calta, Z. Li, Z. Zeng, Y. Zhang, W. Chen, T.T. Roehling, R.T. Ott, M.K. Santala, P.J. Depond, M.J. Matthews, A. V. Hamza, T. Zhu, Additively manufactured hierarchical stainless steels with high strength and ductility, Nat. Mater. 17 (2018) 63–70, https://doi.org/10.1038/NMAT5021.

[28] K.M. Bertsch, G. Meric de Bellefon, B. Kuehl, D.J. Thoma, Origin of dislocation structures in an additively manufactured austenitic stainless steel 316L, Acta Mater. 199 (2020) 19–33, https://doi.org/10.1016/j.actamat.2020.07.063.

[29] M. Gäumann, C. Bezençon, P. Canalis, W. Kurz, Single-crystal laser deposition of superalloys: processing-microstructure maps, Acta Mater. 49 (2001) 1051–1062, https://doi.org/10.1016/S1359-6454(00)00367-0.

[30] W. Kurz, C. Bezençon, M. Gäumann, Columnar to equiaxed transition in solidification processing, Sci. Technol. Adv. Mater. 2 (2001) 185–191, https://doi.org/10.1016/S1468-6996(01)00047-X.

[31] J. Song, Y. Chew, G. Bi, X. Yao, B. Zhang, J. Bai, S.K. Moon, Numerical and experimental study of laser aided additive manufacturing for melt-pool profile and grain orientation analysis, Mater. Des. 137 (2018) 286–297, https://doi.org/10.1016/j.matdes.2017.10.033.

[32] D. Wang, C. Song, Y. Yang, Y. Bai, Investigation of crystal growth mechanism during selective laser melting and mechanical property characterization of 316L stainless steel parts, Mater. Des. 100 (2016) 291–299, https://doi.org/10.1016/j.matdes.2016.03.111.

[33] H.Y. Wan, Z.J. Zhou, C.P. Li, G.F. Chen, G.P. Zhang, Effect of scanning strategy on grain structure and crystallographic texture of Inconel 718 processed by selective laser melting, J. Mater. Sci. Technol. 34 (2018) 1799–1804, https://doi.org/10.1016/j.jmst.2018.02.002.

[34] J.D. Hunt, Steady state columnar and equiaxed growth of dendrites and eutectic, Mater. Sci. Eng. 65 (1984) 75–83, https://doi.org/10.1016/0025-5416(84)90201-5.

[35] S. Guan, K. Solberg, D. Wan, F. Berto, T. Welo, T.M. Yue, K.C. Chan, Formation of fully equiaxed grain microstructure in additively manufactured AlCoCrFeNiTi0.5 high entropy alloy, Mater. Des. 184 (2019), 108202, https://doi.org/10.1016/j.matdes.2019.108202.

[36] S. Guan, D. Wan, K. Solberg, F. Berto, T. Welo, T.M. Yue, K.C. Chan, Additively manufactured CrMnFeCoNi/AlCoCrFeNiTi0.5 laminated high-entropy alloy with enhanced strength-plasticity synergy, Scr. Mater. 183 (2020) 133–138, https://doi.org/10.1016/j.scriptamat.2020.03.032.

[37] S.J. Sun, Y.Z. Tian, H.R. Lin, X.G. Dong, Y.H. Wang, Z.J. Zhang, Z.F. Zhang, Enhanced strength and ductility of bulk CoCrFeMnNi high entropy alloy having fully recrystallized ultrafine-grained structure, Mater. Des. 133 (2017) 122–127, https://doi.org/10.1016/j.matdes.2017.07.054.

[38] F. HajyAkbary, J. Sietsma, A.J. Böttger, M.J. Santofimia, An improved X-ray diffraction analysis method to characterize dislocation density in lath martensitic structures, Mater. Sci. Eng. A 639 (2015) 208–218, https://doi.org/10.1016/j.msea.2015.05.003.

[39] C.A. Bronkhorst, J.R. Mayeur, V. Livescu, R. Pokharel, D.W. Brown, G.T. Gray, Structural representation of additively manufactured 316L austenitic stainless steel, Int. J. Plast. 118 (2019) 70–86, https://doi.org/10.1016/j.ijplas.2019.01.012.

[40] S.J. Sun, Y.Z. Tian, H.R. Lin, H.J. Yang, X.G. Dong, Y.H. Wang, Z.F. Zhang, Transition of twinning behavior in CoCrFeMnNi high entropy alloy with grain refinement, Mater. Sci. Eng. A 712 (2018) 603–607, https://doi.org/10.1016/j.msea.2017.12.022.

[41] C.E. Slone, J. Miao, E.P. George, M.J. Mills, Achieving ultra-high strength and ductility in equiatomic CrCoNi with partially recrystallized microstructures, Acta Mater. 165 (2019) 496–507, https://doi.org/10.1016/j.actamat.2018.12.015.

[42] W.Z. Abuzaid, M.D. Sangid, J.D. Carroll, H. Sehitoglu, J. Lambros, Slip transfer and plastic strain accumulation across grain boundaries in Hastelloy X, J. Mech. Phys. Solids 60 (2012) 1201–1220, https://doi.org/10.1016/j.jmps.2012.02.001.

[43] L. Patriarca, W. Abuzaid, H. Sehitoglu, H.J. Maier, Slip transmission in bcc FeCr polycrystal, Mater. Sci. Eng. A 588 (2013) 308–317, https://doi.org/10.1016/j.msea.2013.08.050.

[44] M. Bönisch, Y. Wu, H. Sehitoglu, Hardening by slip-twin and twin-twin interactions in FeMnNiCoCr, Acta Mater. 153 (2018) 391–403, https://doi.org/10.1016/j.actamat.2018.04.054.

[45] B. Uzer, S. Picak, J. Liu, T. Jozaghi, D. Canadinc, I. Karaman, Y.I. Chumlyakov, I. Kireeva, On the mechanical response and microstructure evolution of NiCoCr single crystalline medium entropy alloys, Mater. Res. Lett. 6 (2018) 442–449, https://doi.org/10.1080/21663831.2018.1478331.

[46] I.V. Kireeva, Y.I. Chumlyakov, Z.V. Pobedennaya, I.V. Kuksgausen, I. Karaman, Orientation dependence of twinning in single crystalline CoCrFeMnNi high-entropy alloy, Mater. Sci. Eng. A 705 (2017) 176–181, https://doi.org/10.1016/j.msea.2017.08.065.